# Chapter 8 Emergent Kagome Spin Configurations in the Basal Plane of BaFe$_{12}$O$_{19}$ as a Function of Temperature

## 8.1 Introduction

The results of X-ray magnetic circular dichroism (XMCD) and magnetization studies on single crystals of BaFe$_{12}$O$_{19}$ (BFO), presented in chapters 3 and 4, provide unambiguous evidence for a significant component of the 3dFe$^{3+}$ spins in the basal plane (i.e., ab-plane) confirming non-collinear nature of the spins. This calls for revisiting the collinear magnetic structure of BFO proposed by Gorter [39]. In chapters 5, 6 and 7, we presented evidence for a succession of five glassy transitions resulting from the freezing of the longitudinal (//c) component of the spins, the transverse ($\perp$c) component of the spins and the freezing of the precession dynamics of the conical magnetic structure using ac susceptibility $\chi(\omega, T)$ studies. Taking analogy with the isostructural compound SrCr$_8$Ga$_4$O$_{19}$ (SCGO), it was tentatively proposed in chapters 5 and 6 that the component of the spin perpendicular to the c-axis (i.e., in the basal plane) would acquire geometrically frustrated kagome spin configuration which may be responsible for the emergence of the spin-glass phases. However, the emergence of the kagome spin configuration in BFO remains to be confirmed. In case of SCGO [18,19,22] and other geometrically frustrated ordered compounds, like pyrochlores [327,328,331,333,334], spinels [337,338] and jarosites [370,425], there is only one spin-glass transition due to the geometry of the lattice on which the magnetic spins are located in the paramagnetic phase itself. In contrast, the five spin-glass phases of BFO result from the long-range ordered (LRO) ferrimagnetic phase of BFO which is stable in the temperature range 250 K $\lesssim$ T < T$_c$ = 714 K. The five spin-glass phases appear successively below 250 K and they coexist

with LRO ferrimagnetic phase all along upto the ground state. This difference between the two systems also needs to be elaborated on.

To address these questions, we have presented the results of neutron powder diffraction (NPD) studies on BFO powder as a function of temperature in this chapter. This study provides evidence for the emergence of two different kagome spin configurations as a function of temperature giving an insight into the microscopic basis of the glassy transitions, discussed in chapters 5, 6 and 7. Apart from providing evidence for emergent geometrical frustration in BFO, we have also addressed the issue of randomness of interactions as both frustration (which is geometrical in the present case) and randomness are required to explain the spin-glass transitions [57,60,61]. Towards this goal, we present results of low-temperature X-ray powder diffraction (XRD) studies which reveal significant magnetoelectric strains in BFO at low temperatures. We also discuss the possible role of unequal Fe-Fe distances in and out of the ab-plane on the exchange anisotropy. Further, implications of change in exchange splitting of the Fe-$e_g$ band around 15 K revealed by the X-ray absorption spectra (XAS) studies at the O K-edge, presented in chapter 4, is also discussed in this chapter in the context of the succession of the spin-glass transitions.

## 8.2   Experimental

The details of the powder synthesis and crystal growth are already given in chapter 2. For neutron and X-ray powder diffraction measurements, sintered pellets of BFO were crushed into fine powders using mortar pastel. The crushed powder was annealed at $600^0$C for 10 hours to remove the strain introduced during crushing. The annealed powder was used for all the powder diffraction studies. The low-temperature NPD data was collected in the temperature range 10 to 300K at a wavelength of 0.207150Å on SPODI, a high-resolution thermal neutron diffractometer at FRM-II, Garching, Germany [187,188].

The temperature-dependent XRD measurements were carried out on an inhouse 18 kW Cu rotating anode based high-resolution powder diffractometer fitted with a monochromator in the diffracted beam (Rigaku, model). The low-temperature attachment, based on a closed cycle He refrigerator, provided by Rigaku was used for varying the sample temperature from 13 K to 300 K.

Rietveld refinement of the nuclear and magnetic structures was carried out using the FullProf suite [186]. The isotropy suite [426] was used to determine the possible magnetic subgroups of the room temperature magnetic structure. Le-bail analysis of the temperature-dependent powder XRD data was also carried out using FullProf suite.

## 8.3    Previous Predictions for Spin Canting in $BaFe_{12}O_{19}$

Based on Mössbauer and magnetization studies on Al, Ga [134,135], In, Sc [135,427] and Mn [428] doped BFO, canting of the magnetic spins at the 12k site has been proposed earlier. However, neutron powder diffraction patterns on Mn doped samples do not reveal any extra reflections for 00$l$ reciprocal lattice row at or around $l = 2n \pm 1$ positions [428] whereas In and Sc doped samples do reveal the extra reflections [134]. It was argued that the absence of spin canting in the neutron powder diffraction patterns could be due to random canting of the spins at the 12k and 2a Wyckoff sites [428]. Theoretical calculations of the single-ion anisotropy of the magnetic ions for different sites in BFO suggest that the single-ion anisotropy of the 12k site $Fe^{3+}$ has negative value whereas it is positive for all other sites [429,430]. The negative value of single-ion anisotropy indicates that anisotropy energy will be maximum when the magnetic spins at the 12k site are parallel to the c-axis [431]. In another theoretical study, it has been pointed out that the magnetic spins at the 12k site are subjected to strong ferromagnetic interactions with spin at the 2a, 2b, 12k sites (all spin-up) and strong anti-ferromagnetic interaction with the spins at the $4f_1$, $4f_2$ sites (all spin down) [432]. Mean-

field calculations of the exchange interactions among the magnetic ions in BFO have revealed that magnetic spins at the 12k site experiences isotropic exchange interaction [433]. It has been argued that the spins at the 12k site plays a crucial role in perturbing the Gorter model for the magnetic structure of BFO [433]. Since magnetic spins at the 12k site are subjected to isotropic exchange interaction while a mixture of ferromagnetic as well as anti-ferromagnetic interactions, the effective field on the 12k site magnetic spins will be very small. The weak effective exchange interaction [433] and the negative value of anisotropy constant of the 12k site [429,430] may lead to canting of spins at this site. Instability of spin direction along the c-axis at the 12k site has been verified by substituting non-magnetic ions at the magnetic sites. It has been found that a very small amount of substitution (3% to 5%) by Al, Ga, Sc, Mn, Zn and In leads to significant canting of the spins at 12k sites [135,192,427,428,434,435]. These observations have led us to assume that the spins at the 12k sites are the most probable candidates for canted spin components discussed in chapters 3 and 4 and are possibly responsible for the transverse and the conical spin-glass transitions discussed in chapters 5, 6 and 7.

## 8.4   Neutron Powder Diffraction Studies

To capture the arrangement of the spins in the ab-plane and along the c-axis due to spin canting at the 12k site, we refined the magnetic and nuclear structures together by Rietveld technique using powder neutron diffraction data. Fig. 8.1 depicts the neutron powder diffraction patterns recorded at a few selected temperatures: 300 K, 250 K, 100 K, 50 K and 10 K. Since the periodicity of the nuclear and magnetic structures is identical (propagation vector k = 0, 0, 0), no additional peak is expected due to the antiparallel arrangement of the $3d^5 Fe^{3+}$ spins at the $4f_1$ and $4f_2$ Wyckoff positions with respect to those at the 2a, 2b, 12k Wyckoff positions, if the spins are aligned exclusively along the
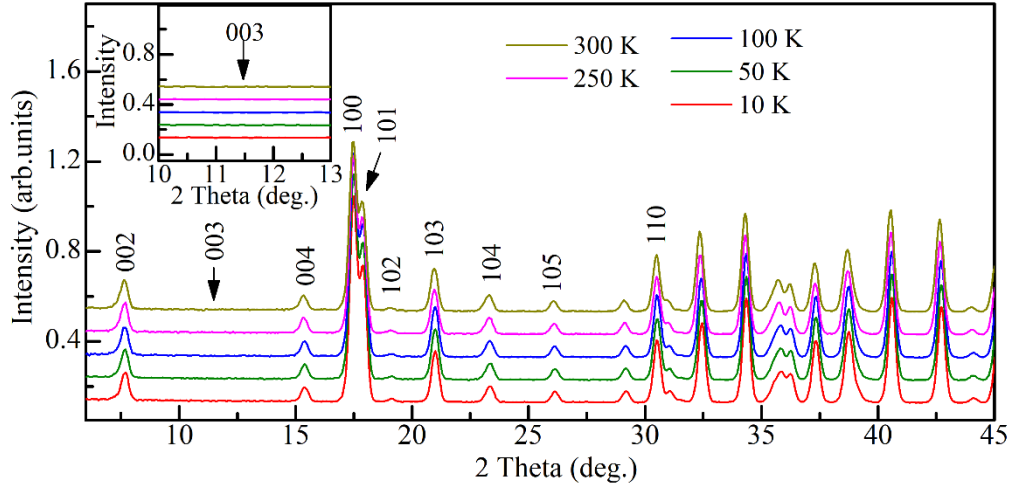
Figure 8.1: Neutron powder diffraction patterns recorded at various temperatures. Inset shows a zoomed around the forbidden of *003* peak position. All the curves are shifted with respect to each other by 0.1 (arbitrary units).

c-axis as per the collinear Gorter model. Additional peak may arise at or around $l = 2n \pm 1$ positions for *00l* type reflections if the spins are canted away from the c-axis [132,133,192,427]. These reflections are forbidden by the nuclear P6$_3$/mmc and magnetic space groups for the collinear Gorter type magnetic structure. In chapters 3 and 4, we presented evidence for spin canting in the 1.2 to 30 K temperature range using XMCD on BFO single crystals. In addition, we gave evidence for the presence of satellite peaks at *003* - $\tau_1$ and *003* + $\tau_2$ positions in single-crystal neutron scattering patterns due to conical magnetic order in chapters 3 and 7 in the temperature range 1.5 to 300 K.

A magnified view of the powder diffraction patterns around the *003* position at various temperatures, however, does not reveal any magnetic satellite peaks (see the inset of Fig. 8.1). The intensity of the satellite peaks is about 1.75% of the intensity of neighbouring intense *004* reflection (see chapter 3 and 7). This intensity is too small to be observed in our neutron powder diffraction patterns on account of higher background count. For example, the background intensity in Fig. 8.1 around the *003* peak position is ~ 33% of the intensity of the neighbouring *004* peak. Thus, there is no possibility of

179

observing the satellite peaks in the neutron powder diffraction patterns shown in Fig. 8.1. However, the other peaks, especially those at lower $2\theta$ angles, also have significant contribution from magnetic scattering which can be captured through Rietveld refinement of both the nuclear and magnetic structures together. Accordingly, we present the results of Rietveld refinements in the following sections using representation group theory approach for the magnetic structure [436].

### 8.4.1    The Irreducible representation for $Fe^{3+}$ in $BaFe_{12}O_{19}$

To refine the magnetic structure, we have determined the magnetic irreducible representations (irreps) [436] for BFO using BasIreps Program [186]. As mentioned earlier, the magnetic ion $Fe^{3+}$ in the unit cell of BFO occupies five different Wyckoff sites labelled as 2a, 2b, $4f_1$, $4f_2$ and 12k. The possible reducible representations for different Wyckoff sites are listed below for each one of these sites in terms of the various irreps. The subscript for each irrep represents the irrep number and the superscript the dimensionality of the irrep.

$\Gamma_{2a} = {}^1\Gamma_2 \oplus {}^1\Gamma_4 \oplus {}^2\Gamma_5 \oplus {}^2\Gamma_6$

$\Gamma_{2b} = {}^1\Gamma_2 \oplus {}^2\Gamma_6 \oplus {}^1\Gamma_9 \oplus {}^2\Gamma_{11}$

$\Gamma_{4f1} = {}^1\Gamma_2 \oplus {}^1\Gamma_4 \oplus {}^2\Gamma_5 \oplus {}^2\Gamma_6 \oplus {}^1\Gamma_7 \oplus {}^1\Gamma_9 \oplus {}^2\Gamma_{11} \oplus {}^2\Gamma_{12}$

$\Gamma_{4f2} = {}^1\Gamma_2 \oplus {}^1\Gamma_4 \oplus {}^2\Gamma_5 \oplus {}^2\Gamma_6 \oplus {}^1\Gamma_7 \oplus {}^1\Gamma_9 \oplus {}^2\Gamma_{11} \oplus {}^2\Gamma_{12}$

$\Gamma_{12k} = {}^1\Gamma_1 \oplus {}^1\Gamma_2 \oplus {}^1\Gamma_3 \oplus {}^1\Gamma_4 \oplus {}^2\Gamma_5 \oplus {}^2\Gamma_6 \oplus {}^1\Gamma_7 \oplus {}^1\Gamma_8 \oplus {}^1\Gamma_9 \oplus {}^1\Gamma_{10} \oplus {}^2\Gamma_{11} \oplus {}^2\Gamma_{12}$

The basis vectors of each irrep for different Wyckoff sites are given in Table 8.1, 8.2 and 8.3. It is evident from the above representations for various Wyckoff sites that the irrep $\Gamma_2$ is common for all the sites. The irrep $\Gamma_2$ has only one basis vector for the magnetic ion at sites 2a, 2b, $4f_1$ and $4f_2$ which can give rise to finite magnetic moment parallel or antiparallel to the c-axis (see Table 8.1 and 8.2) but for the 12k site, $\Gamma_2$ has two basis

Table 8.1: Basis vectors of the irreducible representation $\Gamma_n$ for magnetic ion ($Fe^{3+}$) named as Fe1 at 2a Wyckoff site with fractional coordinate (x=0, y=0, z=0) and Fe2 at 2(b) Wyckoff site with fractional coordinate (x=0, y=0, z=0.25).

| Magnetic Representation | Fe1 (2a) | | Magnetic Representation | Fe2 (2b) | |
|---|---|---|---|---|---|
| | $\begin{pmatrix} x \\ y \\ z \end{pmatrix}$ | $\begin{pmatrix} x \\ y \\ z+1/2 \end{pmatrix}$ | | $\begin{pmatrix} x \\ y \\ z \end{pmatrix}$ | $\begin{pmatrix} x \\ y \\ z+1/2 \end{pmatrix}$ |
| $\Gamma_2$ | $\begin{pmatrix} 0 \\ 0 \\ 1 \end{pmatrix}$ | $\begin{pmatrix} 0 \\ 0 \\ 1 \end{pmatrix}$ | $\Gamma_2$ | $\begin{pmatrix} 1 \\ 0 \\ 0 \end{pmatrix}$ | $\begin{pmatrix} 1 \\ 0 \\ 0 \end{pmatrix}$ |
| $\Gamma_4$ | $\begin{pmatrix} 0 \\ 0 \\ 1 \end{pmatrix}$ | $\begin{pmatrix} 0 \\ 0 \\ -1 \end{pmatrix}$ | $\Gamma_6$ | $\begin{pmatrix} 1 & -1 \\ 2 & 0 \\ 0 & 0 \end{pmatrix}$ | $\begin{pmatrix} 1 & -1 \\ 2 & 0 \\ 0 & 0 \end{pmatrix}$ |
| $\Gamma_5$ | $\begin{pmatrix} 1 & 1 \\ 0 & 2 \\ 0 & 0 \end{pmatrix}$ | $\begin{pmatrix} -1 & -1 \\ 0 & -2 \\ 0 & 0 \end{pmatrix}$ | $\Gamma_9$ | $\begin{pmatrix} 1 \\ 0 \\ 0 \end{pmatrix}$ | $\begin{pmatrix} -1 \\ 0 \\ 0 \end{pmatrix}$ |

Table 8.2: Basis vectors of the irreducible representation $\Gamma_n$ for magnetic ion Fe3 and Fe4 at $4f_{iv}$ (4f1) site with fractional coordinate (x=1/3, y=2/3, z=0.0272) and at $4f_{vi}$ (4f2) site with fractional coordinate (x=1/3, y=2/3, z=0.1904), respectively.

| Magnetic Representation | Fe3 ($4f_1$) and Fe4 ($4f_2$) | | | |
|---|---|---|---|---|
| | $\begin{pmatrix} x \\ y \\ z \end{pmatrix}$ | $\begin{pmatrix} -x \\ -y \\ z+1/2 \end{pmatrix}$ | $\begin{pmatrix} x-y \\ -y \\ -z \end{pmatrix}$ | $\begin{pmatrix} x \\ x-y \\ -z+1/2 \end{pmatrix}$ |
| $\Gamma_2$ | $\begin{pmatrix} 0 \\ 0 \\ 1 \end{pmatrix}$ | $\begin{pmatrix} 0 \\ 0 \\ 1 \end{pmatrix}$ | $\begin{pmatrix} 0 \\ 0 \\ 1 \end{pmatrix}$ | $\begin{pmatrix} 0 \\ 0 \\ 1 \end{pmatrix}$ |
| $\Gamma_4$ | $\begin{pmatrix} 0 \\ 0 \\ 1 \end{pmatrix}$ | $\begin{pmatrix} 0 \\ 0 \\ -1 \end{pmatrix}$ | $\begin{pmatrix} 0 \\ 0 \\ 1 \end{pmatrix}$ | $\begin{pmatrix} 0 \\ 0 \\ -1 \end{pmatrix}$ |
| $\Gamma_5$ | $\begin{pmatrix} 1 & 1 \\ 0 & 2 \\ 0 & 0 \end{pmatrix}$ | $\begin{pmatrix} -1 & -1 \\ 0 & -2 \\ 0 & 0 \end{pmatrix}$ | $\begin{pmatrix} 1 & 1 \\ 0 & 2 \\ 0 & 0 \end{pmatrix}$ | $\begin{pmatrix} -1 & -1 \\ 0 & -2 \\ 0 & 0 \end{pmatrix}$ |
| $\Gamma_6$ | $\begin{pmatrix} 1 & -1 \\ 2 & 0 \\ 0 & 0 \end{pmatrix}$ | $\begin{pmatrix} 1 & -1 \\ 2 & 0 \\ 0 & 0 \end{pmatrix}$ | $\begin{pmatrix} 1 & -1 \\ 2 & 0 \\ 0 & 0 \end{pmatrix}$ | $\begin{pmatrix} 1 & -1 \\ 2 & 0 \\ 0 & 0 \end{pmatrix}$ |
| $\Gamma_7$ | $\begin{pmatrix} 0 \\ 0 \\ 1 \end{pmatrix}$ | $\begin{pmatrix} 0 \\ 0 \\ 1 \end{pmatrix}$ | $\begin{pmatrix} 0 \\ 0 \\ -1 \end{pmatrix}$ | $\begin{pmatrix} 0 \\ 0 \\ -1 \end{pmatrix}$ |
| $\Gamma_9$ | $\begin{pmatrix} 0 \\ 0 \\ 1 \end{pmatrix}$ | $\begin{pmatrix} 0 \\ 0 \\ -1 \end{pmatrix}$ | $\begin{pmatrix} 0 \\ 0 \\ -1 \end{pmatrix}$ | $\begin{pmatrix} 0 \\ 0 \\ 1 \end{pmatrix}$ |
| $\Gamma_{11}$ | $\begin{pmatrix} 2 & 0 \\ 1 & -1 \\ 0 & 0 \end{pmatrix}$ | $\begin{pmatrix} -2 & 0 \\ -1 & 1 \\ 0 & 0 \end{pmatrix}$ | $\begin{pmatrix} -2 & 0 \\ -1 & 1 \\ 0 & 0 \end{pmatrix}$ | $\begin{pmatrix} 2 & 0 \\ 1 & -1 \\ 0 & 0 \end{pmatrix}$ |
| $\Gamma_{12}$ | $\begin{pmatrix} 1 & 1 \\ 0 & 2 \\ 0 & 0 \end{pmatrix}$ | $\begin{pmatrix} 1 & 1 \\ 0 & 2 \\ 0 & 0 \end{pmatrix}$ | $\begin{pmatrix} -1 & -1 \\ 0 & -2 \\ 0 & 0 \end{pmatrix}$ | $\begin{pmatrix} -1 & -1 \\ 0 & -2 \\ 0 & 0 \end{pmatrix}$ |

vectors, one of which gives the moment parallel to the c-axis and the other perpendicular to the c-axis (see Table 8.3(a) and (b)). This suggests that the irrep $\Gamma_2$ can give rise to both collinear and non-collinear magnetic structures. Both $\Gamma_{(2a)}$ and $\Gamma_{2(a \oplus b)}$ irreps, however, have a common magnetic space group P6$_3$/mm'c'. The combination of the other irreps with irrep $\Gamma_2$ can produce other magnetic structures also.

Table 8.3(a): Basis vectors of the irreducible representation $\Gamma_n$ for 6 out of 12 equivalent position of Fe5 at 12k site with fractional coordinate (x=0.168, y=2x, z=-0.1082).

| Magnetic Representation | Fe5 (12k) | | | | | |
|---|---|---|---|---|---|---|
| | $\begin{pmatrix} x \\ y \\ z \end{pmatrix}$ | $\begin{pmatrix} -x \\ -y \\ z-1/2 \end{pmatrix}$ | $\begin{pmatrix} -y \\ x-y \\ z \end{pmatrix}$ | $\begin{pmatrix} -x+y \\ -x \\ z \end{pmatrix}$ | $\begin{pmatrix} x-y \\ x \\ z-1/2 \end{pmatrix}$ | $\begin{pmatrix} y \\ -x+y \\ z-1/2 \end{pmatrix}$ |
| $\Gamma_1$ | $\begin{pmatrix} 1 \\ 0 \\ 0 \end{pmatrix}$ | $\begin{pmatrix} -1 \\ 0 \\ 0 \end{pmatrix}$ | $\begin{pmatrix} 0 \\ 1 \\ 0 \end{pmatrix}$ | $\begin{pmatrix} -1 \\ -1 \\ 0 \end{pmatrix}$ | $\begin{pmatrix} 1 \\ 1 \\ 0 \end{pmatrix}$ | $\begin{pmatrix} 0 \\ -1 \\ 0 \end{pmatrix}$ |
| $\Gamma_2$ | $\begin{pmatrix} 0 & 1 \\ 0 & 2 \\ 1 & 0 \end{pmatrix}$ | $\begin{pmatrix} 0 & -1 \\ 0 & -2 \\ 1 & 0 \end{pmatrix}$ | $\begin{pmatrix} 0 & -2 \\ 0 & -1 \\ 1 & 0 \end{pmatrix}$ | $\begin{pmatrix} 0 & 1 \\ 0 & -1 \\ 1 & 0 \end{pmatrix}$ | $\begin{pmatrix} 0 & -1 \\ 0 & 1 \\ 1 & 0 \end{pmatrix}$ | $\begin{pmatrix} 0 & 2 \\ 0 & 1 \\ 1 & 0 \end{pmatrix}$ |
| $\Gamma_3$ | $\begin{pmatrix} 1 \\ 0 \\ 0 \end{pmatrix}$ | $\begin{pmatrix} 1 \\ 0 \\ 0 \end{pmatrix}$ | $\begin{pmatrix} 0 \\ 1 \\ 0 \end{pmatrix}$ | $\begin{pmatrix} -1 \\ -1 \\ 0 \end{pmatrix}$ | $\begin{pmatrix} -1 \\ -1 \\ 0 \end{pmatrix}$ | $\begin{pmatrix} 0 \\ 1 \\ 0 \end{pmatrix}$ |
| $\Gamma_4$ | $\begin{pmatrix} 0 & 1 \\ 0 & 2 \\ 1 & 0 \end{pmatrix}$ | $\begin{pmatrix} 0 & 1 \\ 0 & 2 \\ -1 & 0 \end{pmatrix}$ | $\begin{pmatrix} 0 & -2 \\ 0 & -1 \\ 1 & 0 \end{pmatrix}$ | $\begin{pmatrix} 0 & 1 \\ 0 & -1 \\ 1 & 0 \end{pmatrix}$ | $\begin{pmatrix} 0 & 1 \\ 0 & -1 \\ -1 & 0 \end{pmatrix}$ | $\begin{pmatrix} 0 & -2 \\ 0 & -1 \\ -1 & 0 \end{pmatrix}$ |
| $\Gamma_5$ | $\begin{pmatrix} 2 & 0 & 0 & 0 & 2 & 0 \\ 0 & 0 & 0 & 0 & 4 & 0 \\ 0 & 0 & 0 & 0 & 0 & 2 \end{pmatrix}$ | $\begin{pmatrix} -2 & 0 & 0 & 0 & -2 & 0 \\ 0 & 0 & 0 & 0 & -4 & 0 \\ 0 & -2 & 0 & 0 & 0 & 2 \end{pmatrix}$ | $\begin{pmatrix} 0 & 2 & 0 & 0 & 2 & 0 \\ -1 & 1 & 0 & 1 & 1 & 0 \\ 0 & 0 & -1 & 0 & 0 & -1 \end{pmatrix}$ | $\begin{pmatrix} 1 & 1 & 0 & 1 & -1 & 0 \\ 1 & -1 & 0 & 1 & 1 & 0 \\ 0 & 0 & 1 & 0 & 0 & -1 \end{pmatrix}$ | $\begin{pmatrix} -1 & -1 & 0 & -1 & 1 & 0 \\ -1 & 1 & 0 & -1 & -1 & 0 \\ 0 & 0 & 1 & 0 & 0 & -1 \end{pmatrix}$ | $\begin{pmatrix} 0 & -2 & 0 & 0 & -2 & 0 \\ 1 & -1 & 0 & -1 & -1 & 0 \\ 0 & 0 & -1 & 0 & 0 & -1 \end{pmatrix}$ |
| $\Gamma_6$ | $\begin{pmatrix} 2 & 0 & 0 & 0 & 0 & 2 \\ 4 & 0 & 0 & 0 & 0 & 0 \\ 0 & 2 & 0 & 0 & 0 & 0 \end{pmatrix}$ | $\begin{pmatrix} 2 & 0 & 0 & 0 & 0 & 2 \\ 4 & 0 & 0 & 0 & 0 & 0 \\ 0 & -2 & 0 & 0 & 0 & 0 \end{pmatrix}$ | $\begin{pmatrix} 2 & 0 & 0 & -2 & 0 & 0 \\ 1 & 0 & -1 & -1 & 0 & -1 \\ 0 & -1 & 0 & 0 & 1 & 0 \end{pmatrix}$ | $\begin{pmatrix} -1 & 0 & -1 & -1 & 0 & 1 \\ 1 & 0 & -1 & 1 & 0 & 1 \\ 0 & -1 & 0 & 0 & -1 & 0 \end{pmatrix}$ | $\begin{pmatrix} -1 & 0 & -1 & -1 & 0 & 1 \\ 1 & 0 & -1 & 1 & 0 & 1 \\ 0 & 1 & 0 & 0 & 1 & 0 \end{pmatrix}$ | $\begin{pmatrix} 2 & 0 & 0 & -2 & 0 & 0 \\ 1 & 0 & -1 & -1 & 0 & -1 \\ 0 & 1 & 0 & 0 & -1 & 0 \end{pmatrix}$ |
| $\Gamma_7$ | $\begin{pmatrix} 0 & 1 \\ 0 & 2 \\ 1 & 0 \end{pmatrix}$ | $\begin{pmatrix} 0 & -2 \\ 0 & -2 \\ 1 & 0 \end{pmatrix}$ | $\begin{pmatrix} 0 & -2 \\ 0 & -1 \\ 1 & 0 \end{pmatrix}$ | $\begin{pmatrix} 0 & 1 \\ 0 & -1 \\ 1 & 0 \end{pmatrix}$ | $\begin{pmatrix} 0 & -1 \\ 0 & 1 \\ 1 & 0 \end{pmatrix}$ | $\begin{pmatrix} 0 & 2 \\ 0 & 1 \\ 1 & 0 \end{pmatrix}$ |
| $\Gamma_8$ | $\begin{pmatrix} 1 \\ 0 \\ 0 \end{pmatrix}$ | $\begin{pmatrix} -1 \\ 0 \\ 0 \end{pmatrix}$ | $\begin{pmatrix} 0 \\ 1 \\ 0 \end{pmatrix}$ | $\begin{pmatrix} -1 \\ -1 \\ 0 \end{pmatrix}$ | $\begin{pmatrix} 1 \\ 1 \\ 0 \end{pmatrix}$ | $\begin{pmatrix} 0 \\ -1 \\ 0 \end{pmatrix}$ |
| $\Gamma_9$ | $\begin{pmatrix} 0 & 1 \\ 0 & 2 \\ 1 & 0 \end{pmatrix}$ | $\begin{pmatrix} 0 & 1 \\ 0 & 2 \\ -1 & 0 \end{pmatrix}$ | $\begin{pmatrix} 0 & -2 \\ 0 & -1 \\ 1 & 0 \end{pmatrix}$ | $\begin{pmatrix} 0 & 1 \\ 0 & -1 \\ 1 & 0 \end{pmatrix}$ | $\begin{pmatrix} 0 & 1 \\ 0 & -1 \\ -1 & 0 \end{pmatrix}$ | $\begin{pmatrix} 0 & -2 \\ 0 & -1 \\ -1 & 0 \end{pmatrix}$ |
| $\Gamma_{10}$ | $\begin{pmatrix} 1 \\ 0 \\ 0 \end{pmatrix}$ | $\begin{pmatrix} 1 \\ 0 \\ 0 \end{pmatrix}$ | $\begin{pmatrix} 0 \\ 1 \\ 0 \end{pmatrix}$ | $\begin{pmatrix} -1 \\ -1 \\ 0 \end{pmatrix}$ | $\begin{pmatrix} -1 \\ -1 \\ 0 \end{pmatrix}$ | $\begin{pmatrix} 0 \\ 1 \\ 0 \end{pmatrix}$ |
| $\Gamma_{11}$ | $\begin{pmatrix} 1 & -1 & 0 & 1 & -1 & 0 \\ 0 & 1 & 0 & 0 & -1 & 0 \\ 0 & 0 & 1 & 0 & 0 & -1 \end{pmatrix}$ | $\begin{pmatrix} -1 & 1 & 0 & -1 & 1 & 0 \\ 0 & -1 & 0 & 0 & 1 & 0 \\ 0 & 0 & 1 & 0 & 0 & -1 \end{pmatrix}$ | $\begin{pmatrix} 0 & 2 & 0 & 0 & 0 & 0 \\ 0 & 1 & 0 & -2 & 1 & 0 \\ 0 & 0 & -2 & 0 & 0 & 0 \end{pmatrix}$ | $\begin{pmatrix} 1 & -1 & 0 & -1 & 1 & 0 \\ 1 & -2 & 0 & -1 & 0 & 0 \\ 0 & 0 & 1 & 0 & 0 & 1 \end{pmatrix}$ | $\begin{pmatrix} -1 & 1 & 0 & 1 & -1 & 0 \\ -1 & 2 & 0 & 1 & 0 & 0 \\ 0 & 0 & 1 & 0 & 0 & 1 \end{pmatrix}$ | $\begin{pmatrix} 0 & -2 & 0 & 0 & 0 & 0 \\ 0 & -1 & 0 & 2 & -1 & 0 \\ 0 & 0 & -2 & 0 & 0 & 0 \end{pmatrix}$ |
| $\Gamma_{12}$ | $\begin{pmatrix} 2 & 0 & 0 & 0 & 2 & 0 \\ 0 & 0 & 0 & 0 & 4 & 0 \\ 0 & 0 & 0 & 0 & 0 & 2 \end{pmatrix}$ | $\begin{pmatrix} 2 & 0 & 0 & 0 & 2 & 0 \\ 0 & 0 & 0 & 0 & 4 & 0 \\ 0 & 0 & 0 & 0 & 0 & -2 \end{pmatrix}$ | $\begin{pmatrix} 0 & 2 & 0 & 0 & 2 & 0 \\ -1 & 1 & 0 & 1 & 1 & 0 \\ 0 & 0 & -1 & 0 & 0 & -1 \end{pmatrix}$ | $\begin{pmatrix} 1 & 1 & 0 & 1 & -1 & 0 \\ 1 & -1 & 0 & 1 & 1 & 0 \\ 0 & 0 & 1 & 0 & 0 & -1 \end{pmatrix}$ | $\begin{pmatrix} 1 & 1 & 0 & 1 & -1 & 0 \\ 1 & -1 & 0 & 1 & 1 & 0 \\ 0 & 0 & -1 & 0 & 0 & 1 \end{pmatrix}$ | $\begin{pmatrix} 0 & 2 & 0 & 0 & 2 & 0 \\ -1 & 1 & 0 & 1 & 1 & 0 \\ 0 & 0 & -1 & 0 & 0 & 1 \end{pmatrix}$ |

Table 8.3(b): Basis vectors of the irreducible representation $\Gamma_n$ for the remaining six equivalent positions of Fe5 at the 12k site with fractional coordinate (x=0.168, y=2x, z=-0.1082).

| Magnetic Representation | Fe5 (12k) | | | | | |
|---|---|---|---|---|---|---|
| | $\begin{pmatrix} x-y \\ -y \\ -z \end{pmatrix}$ | $\begin{pmatrix} y \\ x \\ -z \end{pmatrix}$ | $\begin{pmatrix} -x \\ -x+y \\ -z \end{pmatrix}$ | $\begin{pmatrix} x \\ x-y \\ -z+3/2 \end{pmatrix}$ | $\begin{pmatrix} -x+y \\ y \\ -z+3/2 \end{pmatrix}$ | $\begin{pmatrix} -y \\ -x \\ -z+3/2 \end{pmatrix}$ |
| $\Gamma_1$ | $\begin{pmatrix} 1 \\ 0 \\ 0 \end{pmatrix}$ | $\begin{pmatrix} 0 \\ 1 \\ 0 \end{pmatrix}$ | $\begin{pmatrix} -1 \\ -1 \\ 0 \end{pmatrix}$ | $\begin{pmatrix} 1 \\ 1 \\ 0 \end{pmatrix}$ | $\begin{pmatrix} -1 \\ 0 \\ 0 \end{pmatrix}$ | $\begin{pmatrix} 0 \\ -1 \\ 0 \end{pmatrix}$ |
| $\Gamma_2$ | $\begin{pmatrix} 0 & 1 \\ 0 & 2 \\ 1 & 0 \end{pmatrix}$ | $\begin{pmatrix} 0 & -2 \\ 0 & -1 \\ 1 & 0 \end{pmatrix}$ | $\begin{pmatrix} 0 & 1 \\ 0 & -1 \\ 1 & 0 \end{pmatrix}$ | $\begin{pmatrix} 0 & -1 \\ 0 & 1 \\ 1 & 0 \end{pmatrix}$ | $\begin{pmatrix} 0 & -1 \\ 0 & -2 \\ 1 & 0 \end{pmatrix}$ | $\begin{pmatrix} 0 & 2 \\ 0 & 1 \\ 1 & 0 \end{pmatrix}$ |
| $\Gamma_3$ | $\begin{pmatrix} 1 \\ 0 \\ 0 \end{pmatrix}$ | $\begin{pmatrix} 0 \\ 1 \\ 0 \end{pmatrix}$ | $\begin{pmatrix} -1 \\ -1 \\ 0 \end{pmatrix}$ | $\begin{pmatrix} -1 \\ -1 \\ 0 \end{pmatrix}$ | $\begin{pmatrix} 1 \\ 0 \\ 0 \end{pmatrix}$ | $\begin{pmatrix} 0 \\ 1 \\ 0 \end{pmatrix}$ |
| $\Gamma_4$ | $\begin{pmatrix} 0 & -1 \\ 0 & -2 \\ -1 & 0 \end{pmatrix}$ | $\begin{pmatrix} 0 & 2 \\ 0 & 1 \\ -1 & 0 \end{pmatrix}$ | $\begin{pmatrix} 0 & -1 \\ 0 & 1 \\ -1 & 0 \end{pmatrix}$ | $\begin{pmatrix} 0 & 1 \\ 0 & -1 \\ -1 & 0 \end{pmatrix}$ | $\begin{pmatrix} 0 & 1 \\ 0 & 2 \\ -1 & 0 \end{pmatrix}$ | $\begin{pmatrix} 0 & -2 \\ 0 & -1 \\ -1 & 0 \end{pmatrix}$ |
| $\Gamma_5$ | $\begin{pmatrix} 2 & 0 & 0 & 0 & 2 & 0 \\ 0 & 0 & 0 & 0 & 4 & 0 \\ 0 & 0 & 0 & 0 & 0 & 2 \end{pmatrix}$ | $\begin{pmatrix} 0 & 2 & 0 & 0 & 2 & 0 \\ -1 & 1 & 0 & 1 & 1 & 0 \\ 0 & 0 & -1 & 0 & 0 & -1 \end{pmatrix}$ | $\begin{pmatrix} 1 & 1 & 0 & 1 & -1 & 0 \\ 1 & -1 & 0 & 1 & 1 & 0 \\ 0 & 0 & 1 & 0 & 0 & -1 \end{pmatrix}$ | $\begin{pmatrix} -1 & -1 & 0 & -1 & 1 & 0 \\ -1 & 1 & 0 & -1 & -1 & 0 \\ 0 & 0 & 1 & 0 & 0 & -1 \end{pmatrix}$ | $\begin{pmatrix} -2 & 0 & 0 & 0 & -2 & 2 \\ 0 & 0 & 0 & 0 & -4 & 0 \\ 0 & 0 & 0 & 0 & 0 & 0 \end{pmatrix}$ | $\begin{pmatrix} 0 & -2 & 0 & 0 & -2 & 0 \\ 1 & -1 & 0 & -1 & -1 & 0 \\ 0 & 0 & -1 & 0 & 0 & -1 \end{pmatrix}$ |
| $\Gamma_6$ | $\begin{pmatrix} 2 & 0 & 0 & 0 & 0 & 2 \\ 4 & 0 & 0 & 0 & 0 & 0 \\ 0 & 2 & 0 & 0 & 0 & 0 \end{pmatrix}$ | $\begin{pmatrix} 2 & 0 & 0 & -2 & 0 & 0 \\ 1 & 0 & -1 & -1 & 0 & -1 \\ 0 & -1 & 0 & 0 & 1 & 0 \end{pmatrix}$ | $\begin{pmatrix} -1 & 0 & -1 & -1 & 0 & 1 \\ 1 & 0 & -1 & 1 & 0 & 1 \\ 0 & -1 & 0 & 0 & -1 & 0 \end{pmatrix}$ | $\begin{pmatrix} -1 & 0 & -1 & -1 & 0 & 1 \\ 1 & 0 & -1 & 1 & 0 & 1 \\ 0 & 1 & 0 & 0 & 1 & 0 \end{pmatrix}$ | $\begin{pmatrix} 2 & 0 & 0 & 0 & 0 & 2 \\ 4 & 0 & 0 & 0 & 0 & 0 \\ 0 & -2 & 0 & 0 & 0 & 0 \end{pmatrix}$ | $\begin{pmatrix} 2 & 0 & 0 & -2 & 0 & 0 \\ 1 & 0 & -1 & -1 & 0 & -1 \\ 0 & 1 & 0 & 0 & -1 & 0 \end{pmatrix}$ |
| $\Gamma_7$ | $\begin{pmatrix} 0 & -1 \\ 0 & -2 \\ -1 & 0 \end{pmatrix}$ | $\begin{pmatrix} 0 & 2 \\ 0 & 1 \\ -1 & 0 \end{pmatrix}$ | $\begin{pmatrix} 0 & -1 \\ 0 & 1 \\ -1 & 0 \end{pmatrix}$ | $\begin{pmatrix} 0 & 1 \\ 0 & -1 \\ -1 & 0 \end{pmatrix}$ | $\begin{pmatrix} 0 & 1 \\ 0 & 2 \\ -1 & 0 \end{pmatrix}$ | $\begin{pmatrix} 0 & -2 \\ 0 & -1 \\ -1 & 0 \end{pmatrix}$ |
| $\Gamma_8$ | $\begin{pmatrix} -1 \\ 0 \\ 0 \end{pmatrix}$ | $\begin{pmatrix} 0 \\ -1 \\ 0 \end{pmatrix}$ | $\begin{pmatrix} 1 \\ 1 \\ 0 \end{pmatrix}$ | $\begin{pmatrix} -1 \\ -1 \\ 0 \end{pmatrix}$ | $\begin{pmatrix} 1 \\ 0 \\ 0 \end{pmatrix}$ | $\begin{pmatrix} 0 \\ 1 \\ 0 \end{pmatrix}$ |
| $\Gamma_9$ | $\begin{pmatrix} 0 & -1 \\ 0 & -2 \\ -1 & 0 \end{pmatrix}$ | $\begin{pmatrix} 0 & 2 \\ 0 & 1 \\ -1 & 0 \end{pmatrix}$ | $\begin{pmatrix} 0 & -1 \\ 0 & 1 \\ -1 & 0 \end{pmatrix}$ | $\begin{pmatrix} 0 & -1 \\ 0 & 1 \\ 1 & 0 \end{pmatrix}$ | $\begin{pmatrix} 0 & -1 \\ 0 & -2 \\ 1 & 0 \end{pmatrix}$ | $\begin{pmatrix} 0 & 2 \\ 0 & 1 \\ 1 & 0 \end{pmatrix}$ |
| $\Gamma_{10}$ | $\begin{pmatrix} -1 \\ 0 \\ 0 \end{pmatrix}$ | $\begin{pmatrix} 0 \\ -1 \\ 0 \end{pmatrix}$ | $\begin{pmatrix} 1 \\ 1 \\ 0 \end{pmatrix}$ | $\begin{pmatrix} 1 \\ 1 \\ 0 \end{pmatrix}$ | $\begin{pmatrix} -1 \\ 0 \\ 0 \end{pmatrix}$ | $\begin{pmatrix} 0 \\ -1 \\ 0 \end{pmatrix}$ |
| $\Gamma_{11}$ | $\begin{pmatrix} -1 & 1 & 0 & -1 & 1 & 0 \\ 0 & -1 & 0 & 0 & 1 & 0 \\ 0 & 0 & -1 & 0 & 0 & 1 \end{pmatrix}$ | $\begin{pmatrix} 0 & -2 & 0 & 0 & 0 & 0 \\ 0 & -1 & 0 & 2 & -1 & 0 \\ 0 & 0 & 2 & 0 & 0 & 0 \end{pmatrix}$ | $\begin{pmatrix} -1 & 1 & 0 & 1 & -1 & 0 \\ -1 & 2 & 0 & 1 & 0 & 0 \\ 0 & 0 & -1 & 0 & 0 & -1 \end{pmatrix}$ | $\begin{pmatrix} 1 & -1 & 0 & -1 & 1 & 0 \\ 1 & -2 & 0 & -1 & 0 & 0 \\ 0 & 0 & -1 & 0 & 0 & -1 \end{pmatrix}$ | $\begin{pmatrix} 1 & -1 & 0 & 1 & -1 & 0 \\ 0 & 1 & 0 & 0 & -1 & 0 \\ 0 & 0 & -1 & 0 & 0 & 1 \end{pmatrix}$ | $\begin{pmatrix} 0 & 2 & 0 & 0 & 0 & 0 \\ 0 & 1 & 0 & -2 & 1 & 0 \\ 0 & 0 & 2 & 0 & 0 & 0 \end{pmatrix}$ |
| $\Gamma_{12}$ | $\begin{pmatrix} -2 & 0 & 0 & 0 & -2 & 0 \\ 0 & 0 & 0 & 0 & -4 & 0 \\ 0 & 0 & 0 & 0 & 0 & -2 \end{pmatrix}$ | $\begin{pmatrix} 0 & -2 & 0 & 0 & -2 & 0 \\ 1 & -1 & 0 & -1 & -1 & 0 \\ 0 & 0 & 1 & 0 & 0 & 1 \end{pmatrix}$ | $\begin{pmatrix} -1 & -1 & 0 & -1 & 1 & 0 \\ -1 & 1 & 0 & -1 & -1 & 0 \\ 0 & 0 & -1 & 0 & 0 & 1 \end{pmatrix}$ | $\begin{pmatrix} -1 & -1 & 0 & -1 & 1 & 0 \\ -1 & 1 & 0 & -1 & -1 & 0 \\ 0 & 0 & 1 & 0 & 0 & -1 \end{pmatrix}$ | $\begin{pmatrix} -2 & 0 & 0 & 0 & -2 & 0 \\ 0 & 0 & 0 & 0 & -4 & 0 \\ 0 & 0 & 0 & 0 & 0 & 2 \end{pmatrix}$ | $\begin{pmatrix} 0 & -2 & 0 & 0 & -2 & 0 \\ 1 & -1 & 0 & -1 & -1 & 0 \\ 0 & 0 & -1 & 0 & 0 & -1 \end{pmatrix}$ |

## 8.4.2 Isotropy Subgroups for the Combination of Different Irreducible Representations

To determine the possible combination of the irreps which can give rise to another non-collinear magnetic structure at lower temperatures, we considered the isotropy subgroups of the space group P6$_3$/mm'c' using ISODISTORT package [426]. The isotropy magnetic subgroup tree, so obtained, is shown in Fig. 8.2. The subgroup tree
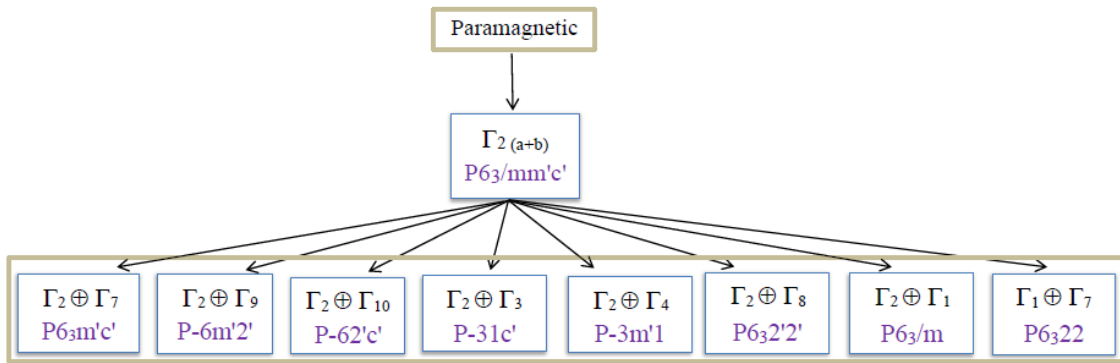
Figure 8.2: Isotropy subgroup tree for the magnetic space group $P6_3/mm'c'$

suggests eight possible magnetic space group corresponding to the irrep combinations $\Gamma_2 \oplus \Gamma_1$, $\Gamma_2 \oplus \Gamma_3$, $\Gamma_2 \oplus \Gamma_4$, $\Gamma_2 \oplus \Gamma_7$, $\Gamma_2 \oplus \Gamma_8$, $\Gamma_2 \oplus \Gamma_9$, $\Gamma_2 \oplus \Gamma_{10}$ and $\Gamma_1 \oplus \Gamma_7$) which are isotropy subgroup of the magnetic space group $P6_3/mm'c'$. A careful analysis of the basis functions of $\Gamma_{2(a \oplus b)}$ as well as the eight possible isotropy subgroups with different irrep combinations shows that all of them can produce canting of the magnetic spins at the 12k Wyckoff site only, in agreement with Mössbauer studies and the theoretical predictions discussed in section 8.3.

### 8.4.3 Details of the Rietveld Refinement

Having identified the various combinations of the irreps that can give rise to non-collinear magnetic structure of BFO using representation theory in conjunction with group-isotropy subgroup considerations, we now proceed to present the results of Rietveld refinements of the average magnetic and nuclear structures. In the refinements, the background was modelled using linear interpolation between the points. The peak shape was modelled using Thompson-Cox-Hasting pseudo-Voigt function. The Full-Width at Half-Maxima (FWHM) of the peaks were modelled using the Caglioti equation [190,191]: $(FWHM)^2 = U\tan^2\theta + V\tan\theta + W$. During the refinement, scale factor, zero displacement, lattice parameters (a, b, c), positional coordinates (x, y, z) and thermal parameters (B) were

allowed to vary while the occupancy of each ion was fixed at their nominal composition value. The initial input structural and thermal parameters were taken from ref. [118].

### 8.4.3.1 Results of Rietveld refinements

Since the Gorter model for the magnetic structure of BFO corresponds to a collinear magnetic structure below 723 K, we have set the second basis vector of the irrep $\Gamma_2$ to zero in the refinement for this magnetic structure. We find that the irrep $\Gamma_{2(a)}$ with only one basis vector gives reasonable average fit down to 10 K. The values of the overall $\chi^2$ and magnetic agreement factor $R_M$ for this model are shown in Fig. 8.3 at various temperatures. It is evident from this figure that the overall $\chi^2$ increases with decreasing temperature. This behaviour of $\chi^2$-value with temperature points towards the possibility of change in the magnetic structure from the collinear model. This implies that the irrep $\Gamma_2$ with only one basis function (i.e., $\Gamma_{2(a)}$) is not enough to explain the real magnetic structure. Therefore, we refined the magnetic structure using both the basis functions of the irrep $\Gamma_2$ i.e., using $\Gamma_{2(a \oplus b)}$. The $\chi^2$-value obtained after refining the magnetic structure at different temperatures using irrep $\Gamma_{2(a \oplus b)}$ are also shown in Fig. 8.3(a). It is evident from this figure that the $\chi^2$-values for the $\Gamma_{2(a \oplus b)}$ non-collinear magnetic structure at 300 K and 250 K are in general lower than those obtained with only one component of $\Gamma_{2(a \oplus b)}$ (i.e., $\Gamma_{2(a)}$). Further, the $\chi^2$-values for $\Gamma_{2(a \oplus b)}$ model at 300 K and 250 K are not significantly different. However, the $\chi^2$-values for this model also starts increasing for temperatures below 250 K. It is evident from Figs. 8.3(b) that the magnetic agreement factor $R_M$ follows the trend similar to that for the $\chi^2$-value with decreasing temperature.

Evidently, the magnetic structure below 250 K requires consideration of other irreps along with $\Gamma_{2(a \oplus b)}$. The subgroup tree in Fig. 8.2 shows eight possible magnetic space groups, along with the corresponding combinations of the various irreps with $\Gamma_{2(a \oplus b)}$, which are isotropy subgroups of the magnetic space group $P6_3/mm'c'$ (i.e., $\Gamma_{2(a \oplus b)}$).
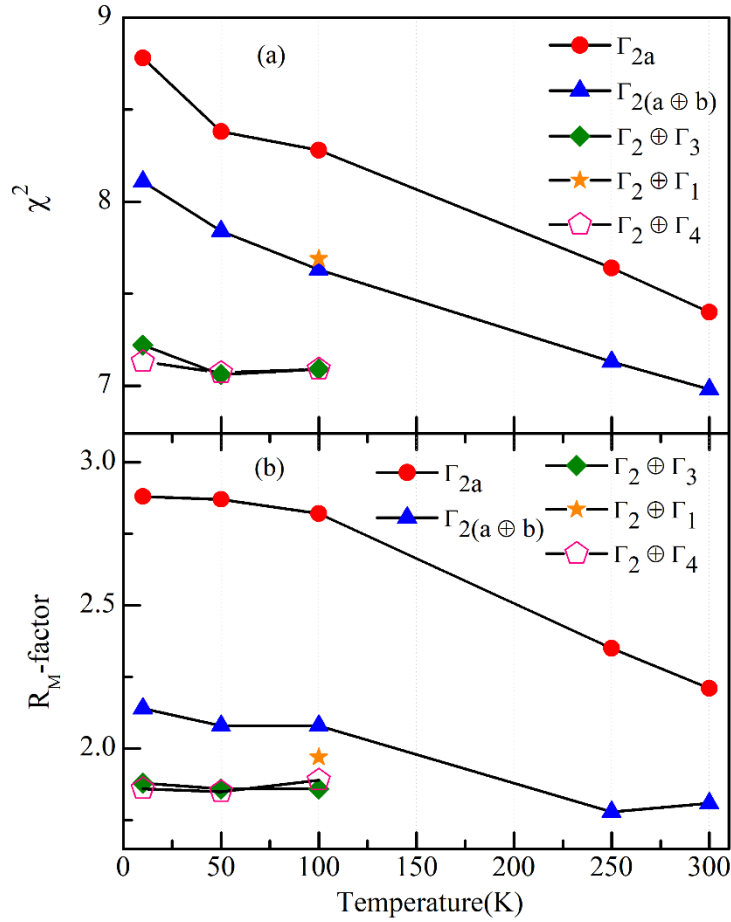
Figure 8.3: The temperature variation of the (a) $\chi^2$ and (b) $R_M$-factor obtained from the Rietveld analysis of neutron diffraction pattern collected at different temperatures.

Accordingly, we refined the magnetic structure using the irrep combinations ($\Gamma_2 \oplus \Gamma_1$), ($\Gamma_2 \oplus \Gamma_3$), ($\Gamma_2 \oplus \Gamma_4$), ($\Gamma_2 \oplus \Gamma_7$), ($\Gamma_2 \oplus \Gamma_8$), ($\Gamma_2 \oplus \Gamma_9$), ($\Gamma_2 \oplus \Gamma_{10}$) and ($\Gamma_1 \oplus \Gamma_7$) corresponding to the eight magnetic isotropy subgroups one by one. As said earlier, all the magnetic isotropy subgroups lead to canting at the 12k site only. We find the refinement of magnetic structure using irrep combinations ($\Gamma_2 \oplus \Gamma_7$), ($\Gamma_2 \oplus \Gamma_8$), ($\Gamma_2 \oplus \Gamma_9$), ($\Gamma_2 \oplus \Gamma_{10}$) and ($\Gamma_1 \oplus \Gamma_7$) give rise to very large $\chi^2$-values in comparison to $\chi^2$-values obtained for ($\Gamma_2 \oplus \Gamma_1$), ($\Gamma_2 \oplus \Gamma_3$) and ($\Gamma_2 \oplus \Gamma_4$) combinations. From the refined structure, we find that $\Gamma_2 \oplus \Gamma_3$ and $\Gamma_2 \oplus \Gamma_4$ irrep combinations give rise to a significant reduction in the $\chi^2$ and $R_M$ values as shown in Fig. 8.3 at 100 K and 50 K. Since the number of

186

refinable parameters for $\Gamma_{2(a \oplus b)} \oplus \Gamma_3$ (magnetic space group P$\bar{3}$1c') and $\Gamma_{2(a \oplus b)} \oplus \Gamma_4$ (magnetic space group P$\bar{3}$m'1) are 3 and 4, respectively, we choose $\Gamma_{2(a \oplus b)} \oplus \Gamma_3$ combination as it gives comparable fit with one less refinable parameter. On lowering the temperature to 10 K, the $\Gamma_{2(a \oplus b)} \oplus \Gamma_4$ gives slightly lower $\chi^2$ and $R_M$ values than those for $\Gamma_{2(a \oplus b)} \oplus \Gamma_3$. However, the difference is not significant enough to choose one or the other keeping in mind that $\Gamma_{2(a \oplus b)} \oplus \Gamma_4$ combination has one additional refinable parameter. We therefore believe that the magnetic structure of BFO at T $\lesssim$ 100 K corresponds to the $\Gamma_{2(a \oplus b)} \oplus \Gamma_3$ combination of irreps. The fits between the observed and calculated profiles, obtained after Rietveld refinement of the magnetic and nuclear structures using irrep $\Gamma_{2(a)}$, $\Gamma_{2(a \oplus b)}$, $\Gamma_{2(a \oplus b)} \oplus \Gamma_3$, and $\Gamma_{2(a \oplus b)} \oplus \Gamma_4$ at 300 K, 250 K, 100 K, 50 K and 10 K, are shown in Fig. 8.4. All these fits are quite satisfactory.

### 8.4.4 Evidence for Geometrical Frustration in the Magnetic Structure of BaFe$_{12}$O$_{19}$

The main finding of the Rietveld refinements is that the magnetic structure of BFO is non-collinear at least for T $\leq$ 300 K in agreement with the single-crystal neutron scattering results presented in chapter 7. For T $\geq$ 300, further neutron diffraction studies are required. This non-collinearity is due to the canting of the magnetic spins at the 12k octahedral sites. We now proceed to discuss the magnetic structure of BFO as a function of temperature on the basis of the results presented in the previous section and compare it with that of the SrCr$_{9p}$Ga$_{12-9p}$O$_{19}$ (SCGO-p) system which has been investigated thoroughly as a function of Ga content [18,22,24,40,238,437].

The spin components along and perpendicular to the c-axis of non-collinear magnetic structure at T $\gtrsim$ 250 K are shown in Figs. 8.5 (a) and (b), respectively. The spin configuration in the ab-plane shown in Fig. 8.5(b) corresponds to kagome lattice consisting of corner shared triangles. For this kagome spin configuration in
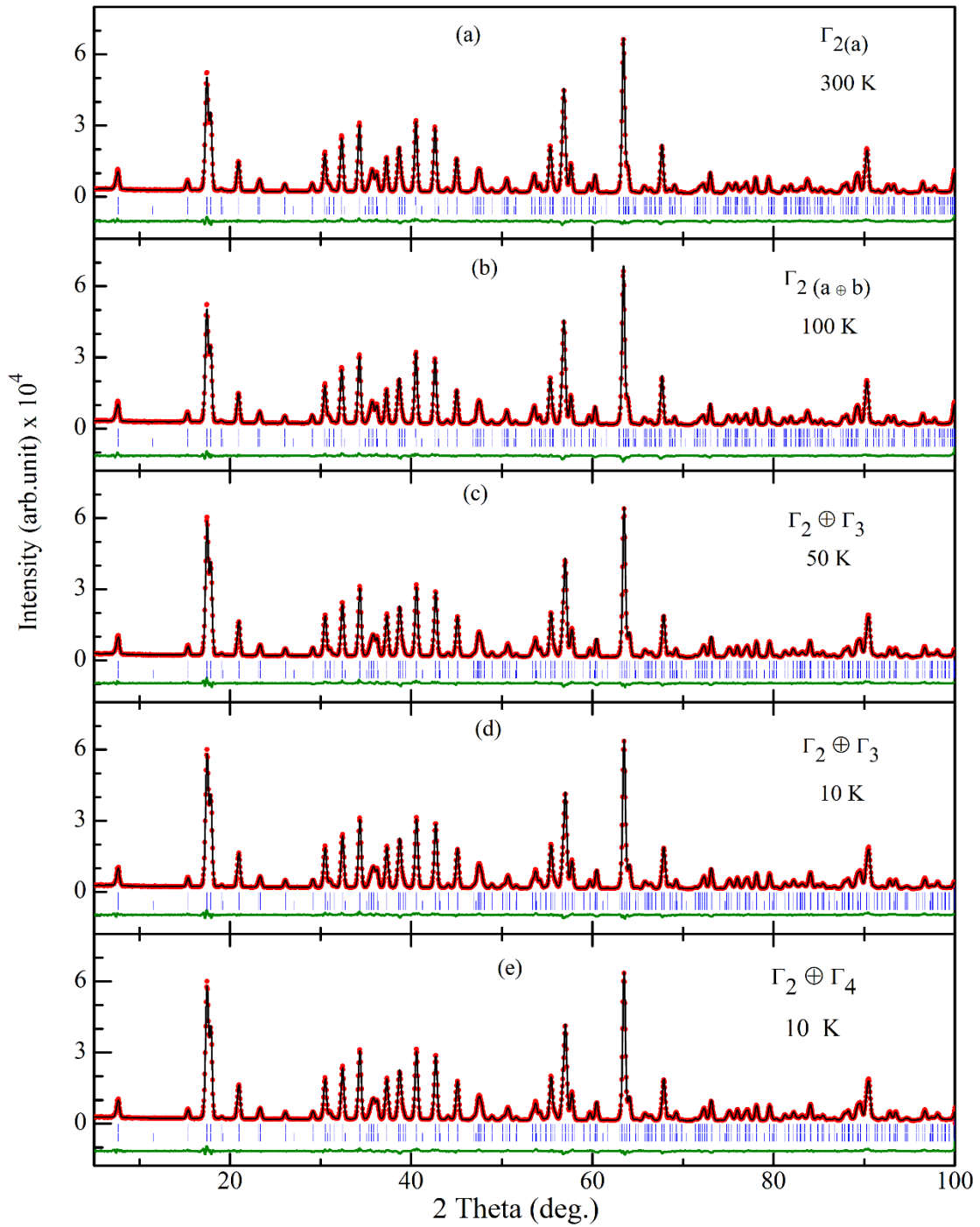
Figure 8.4: Observed (filled red circles), calculated (continuous black line), and difference (bottom green line) profiles obtained from the Rietveld refinement using neutron diffraction data at (a) 300K with $\Gamma_{2a}$, (b) 100K with $\Gamma_{2(a \oplus b)}$, (c) 50K with $\Gamma_2 \oplus \Gamma_3$, (d) 10K with $\Gamma_2 \oplus \Gamma_3$ and (e) 10K with $\Gamma_2 \oplus \Gamma_4$ for $BaFe_{12}O_{19}$. The vertical tick marks above the difference profile represent the Bragg peak positions (blue).
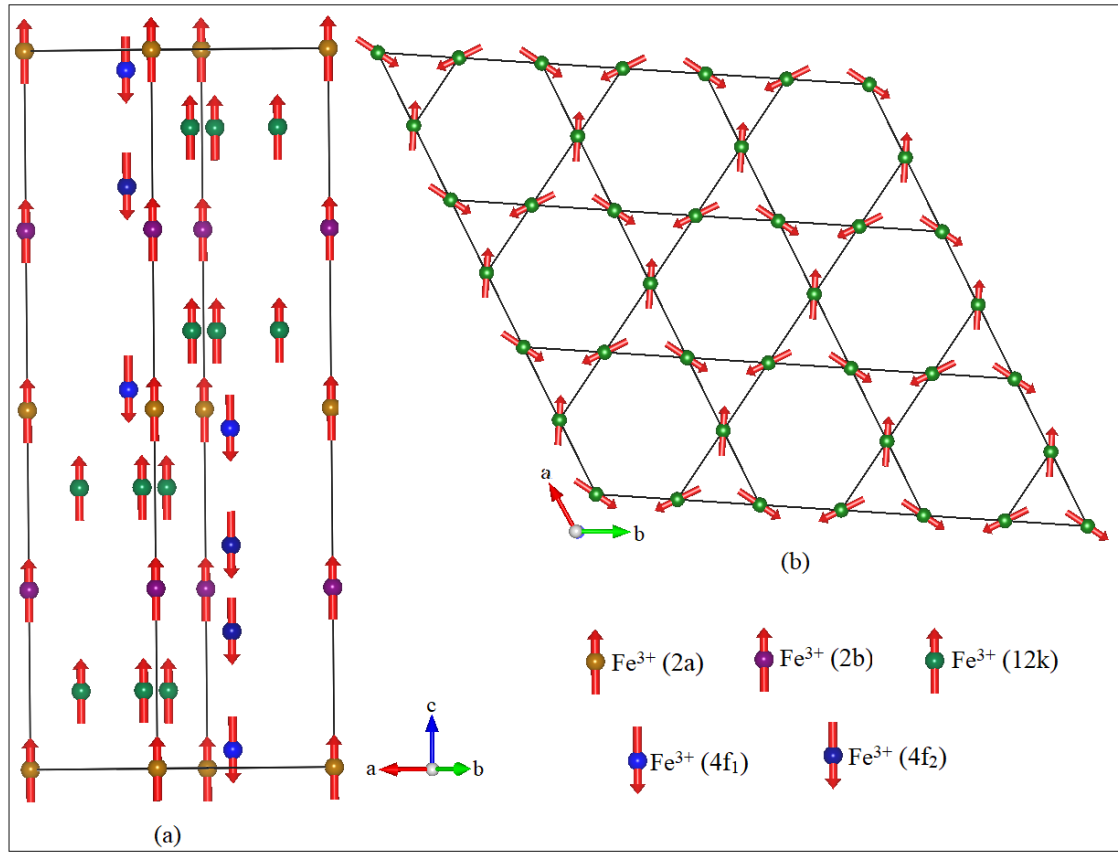
Figure 8.5: Magnetic spin configurations obtained from Rietveld refinement of the magnetic structure using irrep $\Gamma_{2(a \oplus b)}$ (a) longitudinal and (b) transverse components of the canted spins at 300 K and 250 K.

the ab-plane $\sum_{i=1}^{3} S_i = 0$, where $S_1$, $S_2$ and $S_3$ are the three spins all pointing in or out in the corner shared pair of triangles. This configuration has got a degeneracy of two corresponding to two different chiralities [358].

On lowering the temperature below 250 K, the magnetic space group P6$_3$/mm'c' of BFO changes to P$\bar{3}$1c' with $\Gamma_{2(a \oplus b)} \oplus \Gamma_3$ combination of irreps for T $\lesssim$ 100 K. The spin components along the c-axis and within the ab-plane are shown in Figs. 8.6 (a) and (b). The arrangement of the component of the magnetic spins in the ab plane shown in Fig. 8.6(b) correspond to the Wyckoff site 12k only. The magnetic spins at the
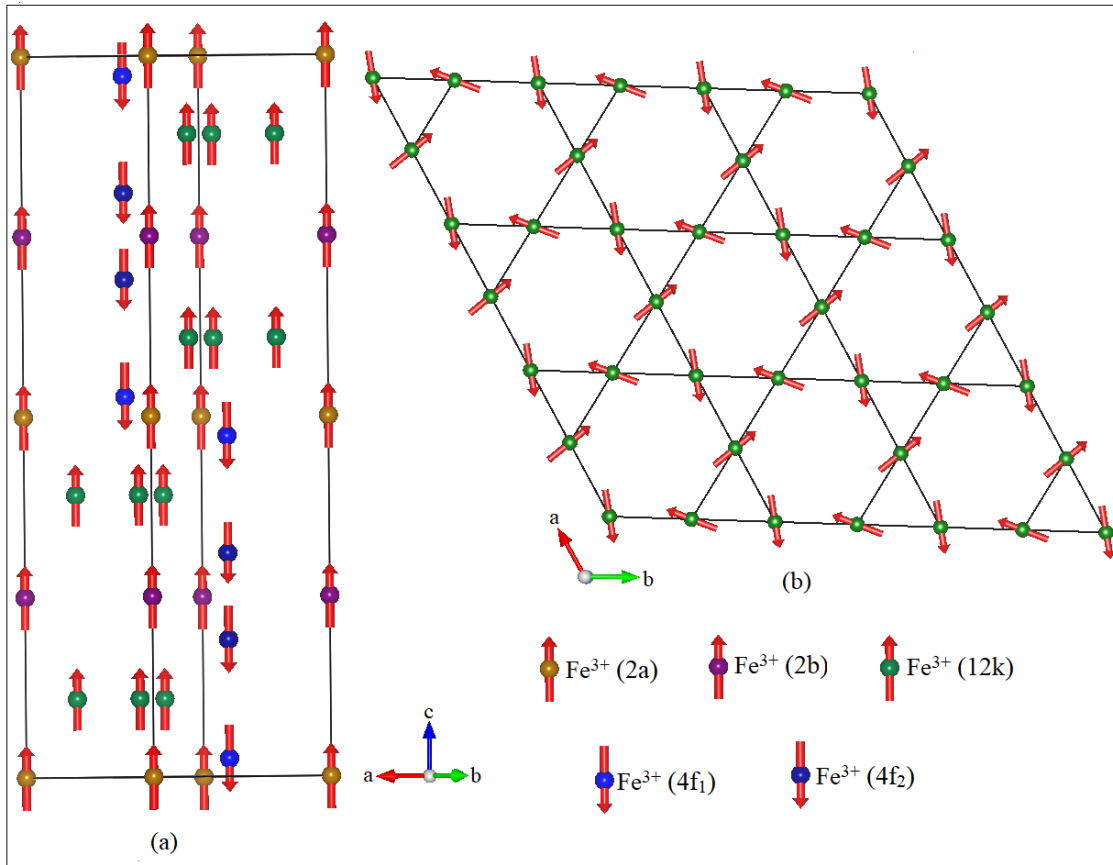
Figure 8.6: Magnetic spin configurations obtained from Rietveld refinement of the magnetic structure using irrep $\Gamma_{2(a \oplus b)} \oplus \Gamma_3$. (a) longitudinal and (b) transverse components of the canted spins at 100 K, 50 K and 10 K.

other Wyckoff sites (2a, 2b, $4f_2$ and $4f_2$) as well as the non-basal component of the spins at the 12k site are all aligned along the c-axis, as in the Gorter model [39]. Thus, the main difference between the magnetic structure of BFO proposed here and that proposed earlier by Gorter [39] is due to the canting of spins at the 12k Wyckoff sites (Fig. 8.6(b)). The kagome antiferromagnet shown in Fig. 8.6(b) is fully frustrated with macroscopic degeneracy [438]. This configuration is similar to that observed in the SCGO system except for the presence of $Ga^{3+}$ ions at some sites [438]. Following the model for SCGO, the successive kagome layers in the ab plane of BFO at T $\lesssim$ 100 K are linked through magnetic spins at the 2a Wyckoff site and form a kagome bilayer configuration linked

through two inverted tetrahedra formed with the spins at the 12k site in the ab plane along with those at the 2a site along the c-axis (see Fig. 8.7). These two inverted corner-shared tetrahedra are like a pyrochlore slab linking the neighbouring kagome layers. The linkage between successive kagome bilayers (12k-2a-12k) is via spins at the $4f_2$ Wyckoff site position at $z = 0.6903$ and $0.8096$ as shown in Fig. 8.7. Every five-layered unit is rotated by $180^0$ about the c-axis to give another similar five-layer block for the 10-layers magnetic spins in BFO. Thus, our Rietveld refinements reveal that fully frustrated kagome bilayer spin configuration emerges as a function of temperature in BFO T ≲ 100 K similar to that in SCGO [438]. We believe that this emergent geometrical frustration,
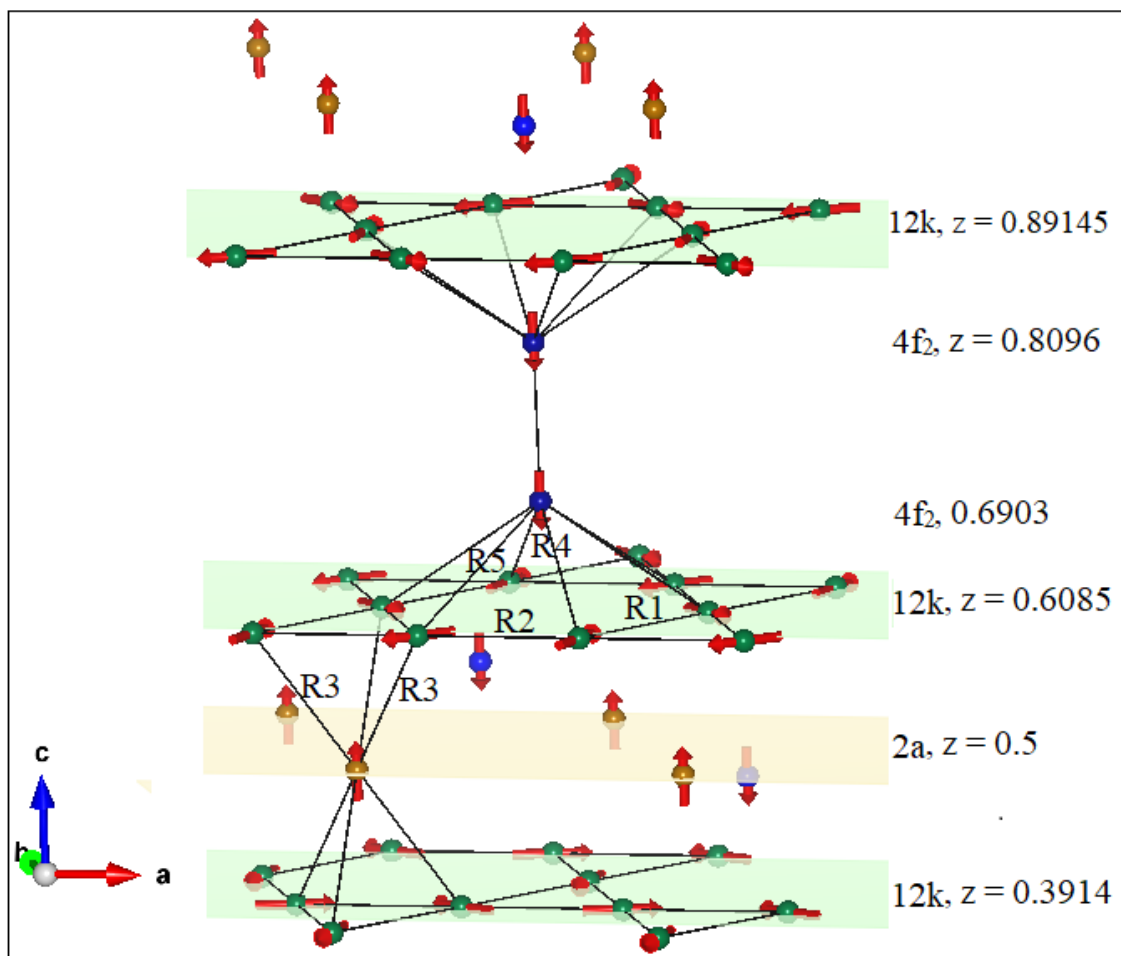


Figure 8.7: Kagome bilayer configuration linked via pyrochlore slabs [19].

191

which persists down to the lowest temperatures (at least 10 K as confirmed in the present study) is at the heart of the emergence of four successive spin-glass transitions discussed in chapter 5.

The five-layer block ($4f_2$-12k-2a-12k-$4f_2$) shown in Fig. 8.7, in case of $SrCr_8Ga_4O_{19}$, has about 14% of the $Cr^{3+}$ replaced with non-magnetic $Ga^{3+}$ at the 12k site whereas the occupancy of $Ga^{3+}$ at the 2a-site is about 4% [237]. In our case, there is no non-magnetic ion in the $Fe^{3+}$ sublattice and hence the occupancy of both the 12k and 2a sites is 100% $Fe^{3+}$. The $4f_1$ Wyckoff site is fully occupied by $Ga^{3+}$ while it has only ~ 13.5% occupy at the $4f_2$ site in SCGO. In BFO, these two sites are also fully occupied by the magnetic ion. Further, the 2b site is occupied by $Ga^{3+}$ only in $SrCr_8Ga_4O_{19}$ but not in BFO and the spins at this site are not involved in exchange linkages for BFO also. However, the kagome bilayer configuration with intervening pyrochlore configuration is common to both BFO and SCGO.

## 8.5    Genesis of Randomness in $BaFe_{12}O_{19}$

As mentioned in the previous chapters, for spin-glass transition one needs both frustration and randomness of interactions. In disordered systems, the source of both frustration and randomness is positional disorder caused by substitutions in the magnetic sublattice with another element/ion, mostly non-magnetic [57,60,61,245,247]. In ordered compounds undergoing spin-glass transitions without any substitutional disorder, such as pyrochlores [327–329,331,334,335], spinels [337] and h-$DyMnO_3$ [249], the source of frustration is the geometry of the lattice of the paramagnetic phase. In case of BFO, we have seen in the previous section, that fully geometrically frustrated kagome spin configuration emerges below $T \lesssim 100$ K. However, this emergent geometrical frustration in the long-range ordered ferrimagnetic phase of BFO, or for that matter, the frozen-in geometrical frustration in other ordered compounds where there is a direct transformation

from paramagnetic phase to the spin-glass phase, is not sufficient to cause spin-glass transition. We need to identify the source of randomness in the few body exchange interactions. As mentioned in earlier chapters, theoretical considerations have revealed that even infinitesimal disorder caused by anisotropy in the exchange interactions due to nearest neighbour bond length variations [332,340,341,346], magnetoelastic strains [341,342] and dipole-dipole interactions between the local spin clusters with intra-cluster geometrical frustration [343] can lift the degeneracy and bring about a phase transition to spin liquid [372,439], spin-ice [361,440] and spin-glass [340,341,345–347] states.

### 8.5.1   Evidence for magnetoelastic strain in $BaFe_{12}O_{19}$

We now proceed to identify the possible source of randomness in case of BFO. For this, we first present the results of the temperature-dependent x-ray powder diffraction studies on BFO in the temperature range 13 K to 300 K. Le-bail refinement of the nuclear structure was carried out for various temperatures using the $P6_3/mmc$ space group for the nuclear structure. These refinements confirm that there is no structural phase transition associated with any of the spin-glass transitions. The results of the Le-bail refinements using the $P6_3/mmc$ space group are shown in Fig. 8.8 for T = 300 K, 100 K, 40 K, 20 K and 13 K. These fits are pretty good confirming that nuclear structure remains $P6_3/mmc$ down to the lowest temperature of our study.

The temperature evolution of the lattice parameters (a, c) and the unit-cell volume (V), obtained using temperature-dependent XRD and NPD data, are shown in Figs. 8.9 and 8.10, respectively.  It is evident from Fig. 8.9 that the lattice parameters 'a' and 'c' as well as the unit cell volume show deviation from linear thermal expansion behaviour below T $\lesssim$ 175 K. Below 100 K, the lattice parameter 'a' becomes nearly temperature independent while 'c' continues to decrease though with a slightly different slope. A
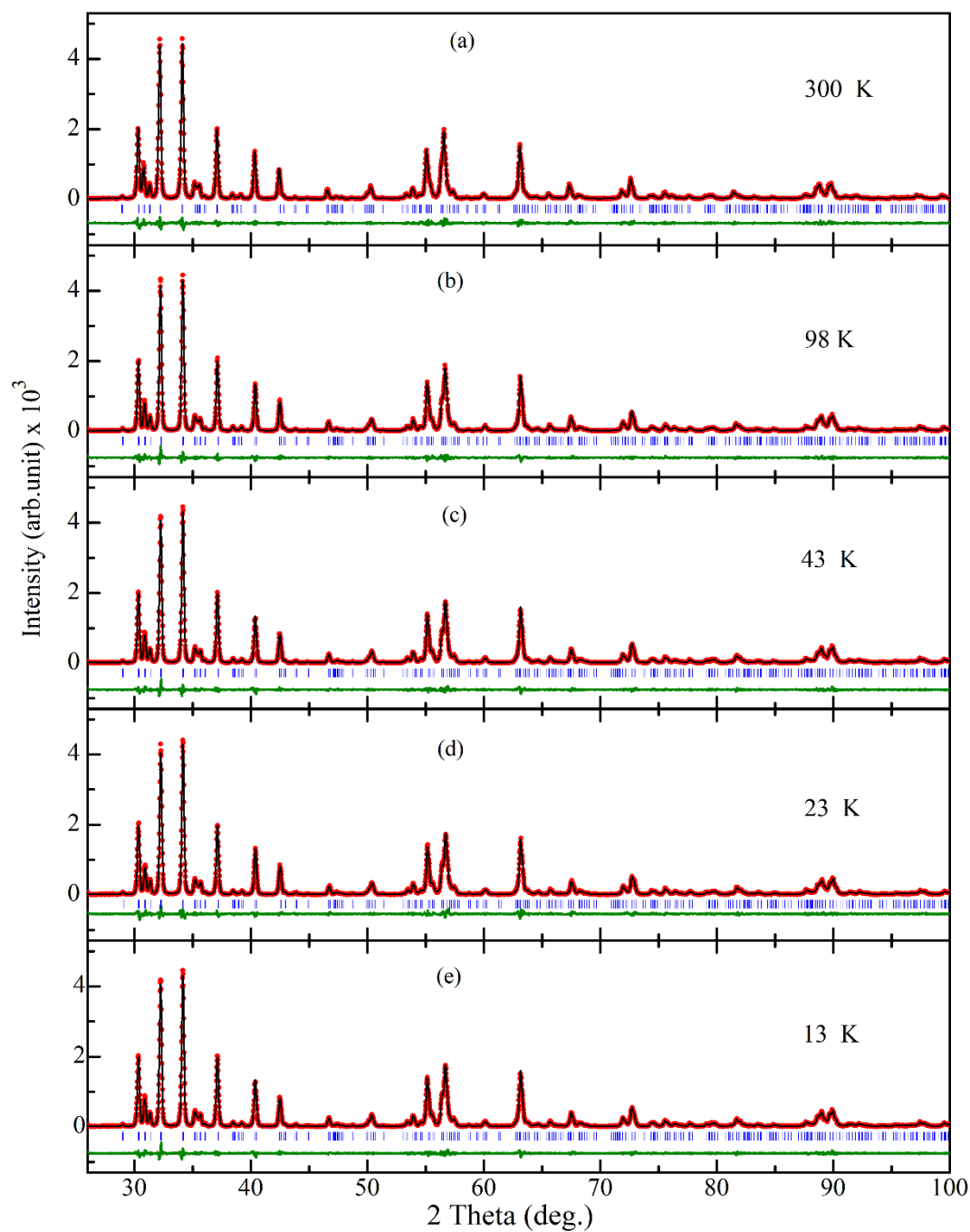
Figure 8.8: Observed (filled red circles), calculated (continuous black line), and difference (bottom green line) profiles obtained from Le-bail refinement using X-ray powder diffraction data at (a) 300 K, (b) 98 K, (c) 43 K (d) 23 K and (e) 13 K for $BaFe_{12}O_{19}$. The vertical tick marks above the difference profile represent the Bragg peak positions (blue).
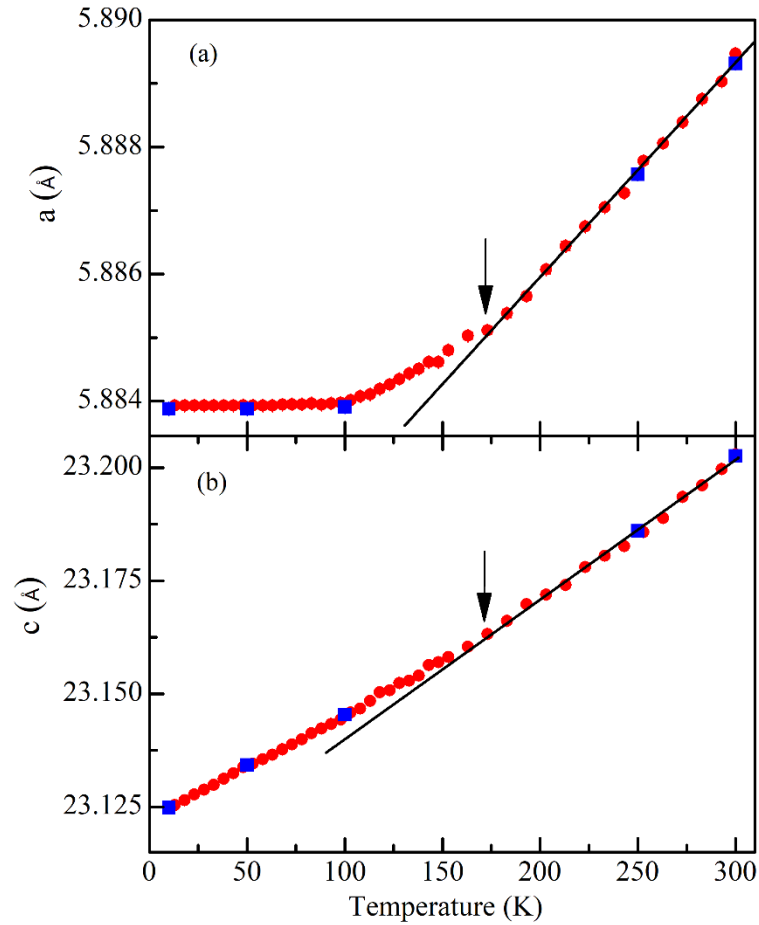
Figure 8.9: The evolution of the lattice parameters (a) 'a' and (b) 'c' with temperature: filled red circle is from the XRD data. Filled squares (blue colour) are from NPD data discussed in the section 8.4.3.1. The solid black line is the straight-line fit.

similar deviation in the c-parameter has been reported earlier [441] where this was linked with the local magnetic field of $Fe^{3+}$ ion. The Rietveld results of the magnetic structure using NPD data, presented in the previous section, have revealed a change in the magnetic space group from $P6_3/mm'c'$ to $P\bar{3}1c'$ in the temperature range 250 to 100 K. The fifth spin-glass transition, discussed in the preceding chapter, occurs in this temperature range. We believe that deviation observed in the lattice parameters 'a' and 'c' around 175 K is due to spin-lattice coupling associated with the glassy transition around 175 K.

In order to see the effect of anomalous behavior of the lattice parameters and magnetic correlations on the unit-cell volume, we have used the Debye- Grüneisen model for the lattice specific heat to calculate the anharmonic part of lattice vibration which contributes to the unit cell volume (V) as per the relationship [442,443]:

$$V = V(T{=}0) + \frac{9\gamma Nk_B}{B} T \left(\frac{T}{\theta_D}\right)^3 \int_0^{T/\theta_D} \frac{x^3}{(e^x-1)} dx, \qquad \text{.......(8.1)}$$

where V(T=0) is the volume at 0 K, $\theta_D$ is the Debye temperature, $\gamma$ is the Grüneisen parameter and *B* is the bulk modulus. The least-squares fit corresponding to Equation (8.1) to data points is shown in Fig. 8.10 using solid black line. The Debye temperature and V(T=0) values are found to be $538 \pm 3$ K and $693.7 \pm 0.01$ Å$^3$, respectively. It is evident from Fig. 8.10 that the calculated unit cell volume deviates from the experimental
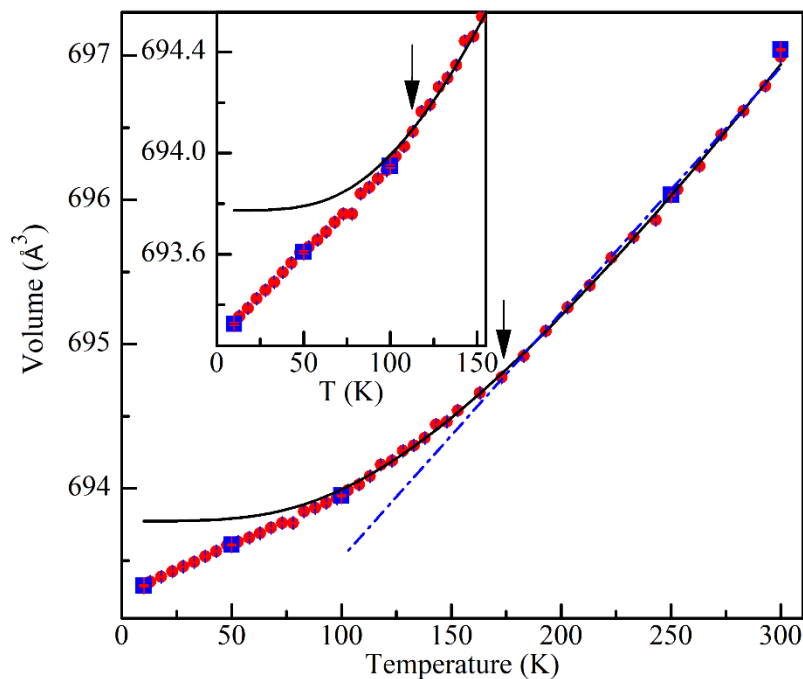


Figure 8.10: Variation of the unit-cell volume with temperature: filled red circle is the XRD data, filled square (blue colour) is NPD data and solid black line is the fit for Debye Grüneisen equation. The broken line through the data points is the straight-line fit.

value of unit cell volume below ~ 125 K. This is shown more clearly in the inset of Fig. 8.10 on a magnified scale. The significant deviation from the theoretically expected phonon contributions to the unit cell volume below ~ 125 K shows the presence of magnetoelastic strains which may be the source of randomness in the few body exchange interactions leading to spin- glass transitions in the presence of emergent geometrical frustration in BFO at low temperatures (T $\lesssim$ 125 K).

The magnetoelastic volume strain ($\Delta V/V$) in many compounds exhibits quadratic dependence on the spontaneous magnetization ($M_s$) [74,442,443] which is known as magneto-volume effect [444]. In order to verify the magneto-volume effect, we measured spontaneous magnetization using M-H plots for the powder samples at various temperatures. The M-H plots for one quadrant are shown in Fig. 8.11 for a few selected temperatures. The variation of the bulk strain ($\Delta V/V$) with $M_s^2$ is shown in Fig. 8.12. It

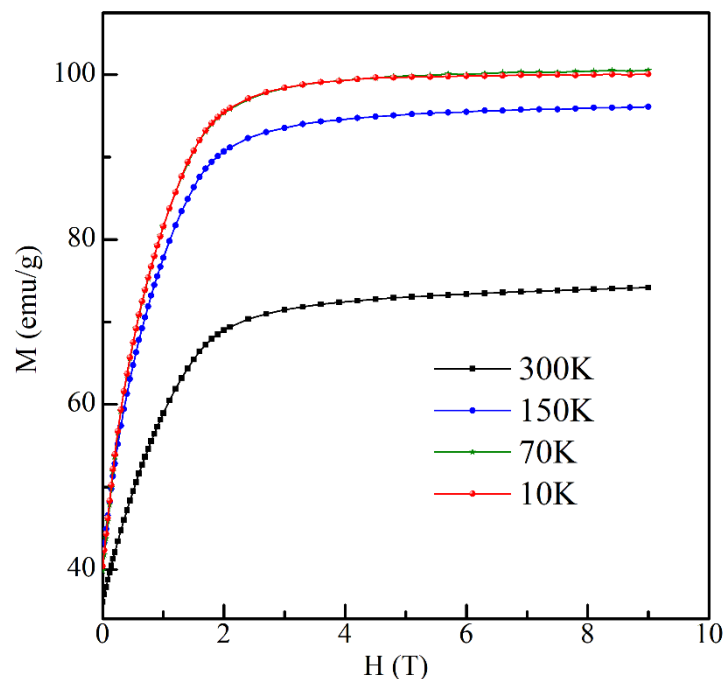

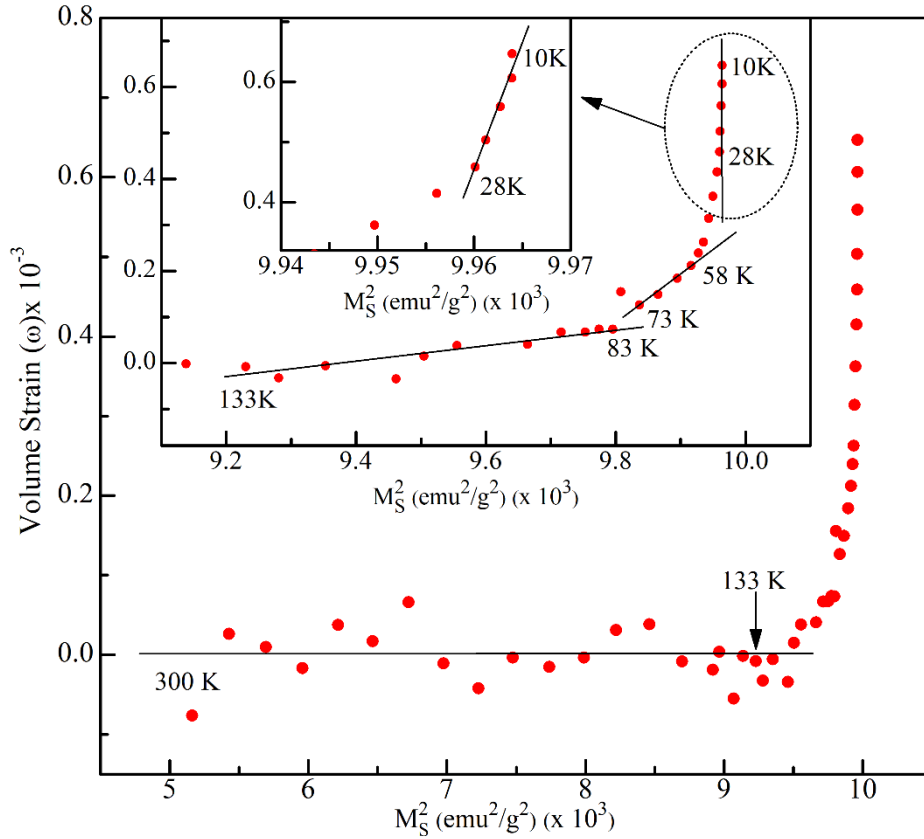Figure 8.11: Variation of magnetization with dc magnetic field.

Figure 8.12: the variation of volume strain $\omega_S$ (i.e., $\Delta V/V$) versus the square of spontaneous magnetization ($M_S^2$) obtained from temperature-dependent M-H loop.

reveals three temperature regions in which $\Delta V/V$ shows linear dependence on $M_s^2$. The first region corresponds to the glassy phase resulting below 175 K while the remaining two regions may be related to the other spin-glass states discussed in the previous chapters. This suggests that the conical spin-glass phase below 175 K shows magneto-volume effect. The slope of $\Delta V/V$ versus $M_s^2$ plot increases below 83 K and finally becomes very steep below 28 K. All these suggest the presence of magnetoelastic strains in BFO below 175 K (see Figs. 8.9 and 8.10). Such strains by virtue of their long-range effects may provide the randomness in the few body exchange interactions which along with emergent geometrical frustration in BFO may stabilise the spin-glass phases in ordered compounds, as shown by various workers theoretically [332,340,341,346]. In the presence of such random strains, Andreanov et al. [332] have shown that the

geometrically frustrated systems do not show deviations from conventional spin-glass results. The successive freezing of the transverse and longitudinal components of the spins below the conical glass transition are, on the other hand, in excellent agreement with the theoretical predictions for conventional Heisenberg systems with negative single-ion anisotropy [67]. This single-ion anisotropy for the 12k site is known to be negative for BFO [429,430] as discussed in section 8.3. After the first round of such freezing, BFO intriguingly shows a similar freezing again at lower temperatures, the origin of which we discuss in the next section.

### 8.5.2 Role of the Exchange Anisotropy

As pointed out in chapter 4, the anisotropy in magnetisation grows with decreasing temperature below $T_c$ until the onset of spin-glass transition around 45 K (see Fig. 4.3). The Curie-Weiss fits for the variation of $M_{\perp c}$ and $M_{//c}$ with temperature also gives different values for the Curie-Weiss temperatures ($\Theta_{CW}$) (see Fig. 4.1). As per molecular field theory, it clearly points towards variation in exchange interactions $J_{\perp c}$ and $J_{//c}$ perpendicular to and along the c-axis. Such an anisotropic exchange interaction has also been shown to lift the degeneracy of the geometrically frustrated magnetic lattices and stabilise a new phase [332]. We believe that apart from the magnetoelastic strains, the exchange anisotropy may also play important role in stabilising the spin-glass phases, especially at lower temperature. The role of exchange anisotropy for disordered Heisenberg systems has been investigated and it has been shown that such an anisotropy can lead to a succession of two lines, the Almeida-Thouless (A-T) and Gabay-Toulouse (G-T), in the T-H plane [236]. The anisotropy in exchange interactions is also anticipated from the variation in the nearest neighbour bond lengths, R1, R2, R3, R4 and R5, shown in Fig. 8.7 for BFO, are 2.916(0) Å, 2.9693(2) Å, 3.479(2) Å, 3.494(2) Å and 3.4935(1) Å, respectively, confirming the presence of exchange anisotropy in BFO. In chapter 4, the

analysis of XAS spectra recorded for the normal incidence (NI) geometry at the O K-edge revealed that the exchange splitting of the $e_g$ band between 15.5 K and 5.5 K changes by about 0.17 eV. This indicates that the exchange interactions may change at lower temperatures. We believe that the second round of freezing of the longitudinal and transverse components of the spins with $T_{SG//c} \sim 15$ K and $T_{SG\perp c} \sim 4$ K, after the first round of freezing at $T_{SG//c} \sim 25$ K and $T_{SG\perp c} \sim 46$ K, respectively, may be linked with the change in the exchange anisotropy around 15 K. All these possibilities need to be looked into in any future theoretical investigation on the origin of multiple spin-glass transitions in BFO.

### 8.5.3   The Origin of the Incommensurate Conical Spin-Glass Phase

In chapter 7, we presented evidence a fifth spin-glass with $T_{SG} \sim 173$ K using neutron scattering and bulk magnetic studies. It was shown that incommensurability of the block conical modulation increases suddenly below $T_{SG} \sim 173$ K. While the intensity of the satellite peaks shows a dip at the same temperature suggesting involvement of conical magnetic ordering in the glassy freezing. The emergent kagome spin configuration at 300 K and 250 K does not have macroscopic degeneracy. The spin configuration shown in Fig. 8.5(b) is doubly degenerate corresponding to left and right-handed chiralities. This implies that the dynamics of the conical modulation may be influence by the chiralities of the spin configuration either only in the ab-plane or out of the ab-plane involving both the longitudinal and transverse components of the spins. The former case corresponds to 2D X-Y Heisenberg system while the latter corresponds to 3d Heisenberg system with vector chiralities $\vec{k} = \vec{s_i} \times \vec{s_j}$, where $\vec{s_i}$ and $\vec{s_j}$ are the neighbouring spins in the plane, and scalar chiralities $k = \vec{s_i} . (\vec{s_j} \times \vec{s_k})$, respectively. Our case corresponds to scalar chiralities which has got $Z_2$ chiral degeneracy corresponding to left-handed and right-handed chiralities while spins have SO(3) spin rotation symmetry. Since

a degeneracy of two is not sufficient to cause the spin-glass transition, which requires macroscopic degeneracy, the origin of the glass transition with $T_{SG} \sim 173$ K needs to be looked into in the light of the chirality scenario discussed by Kawamura and his co-workers in a series of papers [384,416,445–452]. It has been argued by these workers [384] that for nearly isotropic 3d Heisenberg systems, chiralities and spin components may get decoupled and lead to chiral glass transition at a temperature higher than the spin-glass transition temperature. Assuming the spins at the 12k site experience isotropic exchange interactions (see section 8.3), the glass transition around 173 K may be linked with the decoupling of the chirality from the spins. However, theory predicts that the spin-glass transition temperature $T_{SG}$ may be 10 to 15% lower than the chiral glass transition temperature $T_{CG}$. In our case, the difference between the glass transition temperature for the $\sim 173$ K transition and the next spin-glass transition temperature $\sim 50$ K is too large. We, therefore, believe that the origin of the $\sim 173$ K glassy transition is entirely different from the remaining four lower temperature glass transitions. In the light of the neutron scattering results presented in chapter 7, we also believe that this transition this transition is linked with the conical ordering involving all the three components and not just the transverse or longitudinal components. Also, exchange anisotropy for the 12k site may be non-zero since the number of ferromagnetic exchange bonds exceeds the number of antiferromagnetic bonds for the 12k site. For the weakly anisotropic 3D Heisenberg system, the theory predicts recoupling of the chiral and spin degree of freedom. As a result, the chiral glass transition would appear as a standard spin-glass transition. A Gabay Toulouse (G-T) like line in the T-H plane for the shift of the glass transition temperature is predicted for such recoupled scenario at high fields whereas at extremely low fields, the theory predicts the shift along the Almeida-Toulouse (A-T) line. In our case, the shift observed for $H \gtrsim 100$ Oe is along the G-T line (see Fig. 7.10). More

measurements preferably using ac $\chi'(T)$ data, under low dc bias ($H \ll 100$ Oe) is required to verify the crossover from A-T to G-T line with increasing field in any future investigation to confirm the applicability of the theoretical prediction involving chirality scenario.

## 8.6   Conclusions

(1). The deviation from collinear Gorter model is primarily due to canting of the spins at the 12k sites, leaving the spins at other sites aligned parallel or antiparallel to the c-axis.

(2). Evidence for the presence of fully frustrated kagome spin configuration at $T \lesssim 100$ K in BFO was presented using Rietveld analysis of the temperature-dependent NPD data. Rietveld refinement gives only the average spin configurations. In real systems, the spins would show disorder from the average configuration due to the frustrated exchange interactions. Such a disorder is expected to lead to magnetic diffuse scattering [314,453]. Although not included in the thesis, the preliminary studies on BFO single crystals have revealed significant magnetic diffuse scattering around the Bragg peak positions at 30 K.

(3). Using temperature-dependent powder XRD studies, we have shown the presence of significant anisotropic magnetoelastic strains below 175 K in BFO. We have also confirmed magneto-volume effect in different temperature ranges corresponding to the various spin-glass phases of BFO. These strains may provide randomness to the few body exchange interactions required for lifting the degeneracy of the fully frustrated emergent kagome spin configuration at $T \lesssim 100$ K as per the existing theories of the spin-glass transitions in geometrically frustrated ordered compounds.

(4). We have presented some suggestion for the likely genesis of four successive spin-glass transitions of BFO below $T < 100$ K involving either the transverse or the

longitudinal spin components in terms of single-ion anisotropy and the anisotropic exchange interactions.

(5). We have also presented a brief discussion on the genesis of the spin-glass transition around 173 K discussed in the previous chapter. We proposed that this transition is independent of the remaining four spin-glass transitions and may be linked with the theoretically predicted chirality scenario for the weakly anisotropic 3D Heisenberg systems due to the involvement of the conical magnetic order in this transition.